Transport in strongly driven heterostructures and bound-state-induced dynamic resonances

Wenjun Li and L. E. Reichl
Center for Studies in Statistical Mechanics and Complex Systems, The University of Texas at Austin, Austin, Texas 78712
(Received 2 March 2000; revised manuscript received 26 May 2000)

We consider driven heterostructures involving both homogeneous potential modulation and dipole-type modulation regions, which can properly model experimental devices. Numerical results agree with photon-assisted-tunneling experiments. We observe the experimentally detectable bound-state-induced dynamic transmission resonances. Applications in quantum measurements and quantum switching devices are discussed.

I. INTRODUCTION

The study of transport in intensely driven mesoscopic systems is a growing field[1–13] due to the development of a new class of nanostructure devices, such as terahertz high-frequency detectors,[14] quantum electron pumps,[15] and quantum resonant tunneling diodes and triodes for use in quantum communication and quantum computation.[16] Newly developed techniques, such as the free-electron laser (FEL),[1] make experimental studies possible. The quantum photon-assisted-tunneling (PAT) effect has been observed in quantum superlattices,[1] resonant tunneling diodes,[3] and split gate defined quantum dots.[4] It is believed that in the near future, a reliable and accurate theoretical procedure must be developed for experimental data analysis, as well as application device design. For strong oscillating fields, Floquet theory[17] has had some success in treating the dynamics of such systems. When considering transport through a system with spatially homogeneous potential oscillations [with $V(x,t) = V_1 \cos \omega t$], Floquet theory is straightforward, and has been well studied during the past decade. The more practical dipole-type oscillations that occur in most of the experimental setups [with $V(x,t) = eF_1 x \cos \omega t$], have also been treated with time-dependent perturbation theory[6] and using Floquet theory (for example, Refs. 8–11). However, a common simplification in these models is to assume that a uniform oscillating field exists for all space, neglecting the fact that the type of the oscillation (but not the frequency) actually changes at the boundaries. As sketched in Fig. 1, when our semiconductor device is coupled to an optical radiation (with the electric polarization direction parallel to the multilayer growth direction[3]), or subjected to an ac voltage, we create both homogeneous potential modulation and dipole-type potential modulation in different regions (see shadowed areas in Fig. 1). There then arises the question of how to deal with the boundary conditions as will be discussed later in this paper.

Our numerical results are in qualitative agreement with the PAT experiments.[3] The PAT effect originates from the interaction of traveling electrons with the oscillating field. By absorbing or emitting photons, the incident electrons are able to transit to new energy channels. If those channels happen to correspond to resonant tunneling, enhancement of the transmission current can be observed, appearing as additional peaks in the *I-V* curve, as shown in many PAT measurements.[1–4] In this paper, we show that when the incident electrons transit to system bound states, a new type of transmission resonance can occur with very different features. Instead of showing a transmission peak as is the case for PAT, the transition to bound state generally is accompanied by a sharp transmission dip (or a peak-dip pair). This can be observed according to the transmission coefficient pattern as well as in the *I-V* curve. This effect has not been reported in experiments yet.

II. FLOQUET SCATTERING

Let us consider a sequence of semiconductor barriers (wells) along the x direction (see Fig. 1, which is similar to the experimental setups in Refs. 1, 2, and 3). Current flows into and out of the device through Ohmic contacts.[18] The Schrödinger equation can be written as

$$i\hbar \frac{\partial}{\partial t}\Psi(\mathbf{r},t) = -\frac{\hbar^2}{2\mu}\nabla^2\Psi(\mathbf{r},t) + V(x,t)\Psi(\mathbf{r},t), \qquad (1)$$

where $\mathbf{r}=(x,y,z)$. Since the potential varies just in the x direction, Eq. (1) is separable. We can decompose $\Psi(\mathbf{r},t)$ into the longitudinal (x) and transverse (y and z) parts:

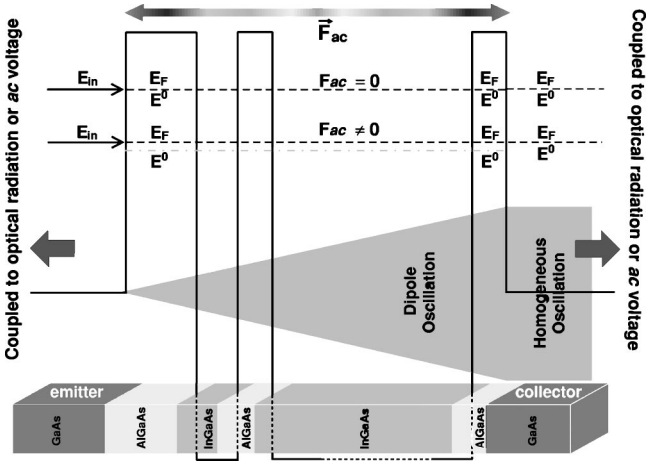

FIG. 1. Semiconductor heterosturcture and the band diagram. Shadowed regions represent the potential modulations due to the oscillating field. The left emitter region is chosen as the potential reference. In the collector region the homogeneous oscillation amplitude represents the coupling strength to the external radiation (or ac voltage). The potentials in the middle barrier/well regions are modulated linearly.

$$\Psi(\mathbf{r},t)=\psi(x,t)\phi(y,z,t). \tag{2}$$

Then the motion along the x direction is governed by a one-dimensional (1D) Schrödinger equation:

$$i\hbar\frac{\partial}{\partial t}\psi(x,t)=-\frac{\hbar^2}{2\mu}\frac{\partial^2}{\partial x^2}\psi(x,t)+V(x,t)\psi(x,t). \tag{3}$$

Due to the external oscillating field, the potential in each barrier (well) can be modulated periodically. Let us write the potential in the ith region in a general form,

$$V^i(x,t)=V_0^i+eF_0^ix+V_1^i\cos(\omega t)+eF_1^ix\cos(\omega t), \tag{4}$$

where V_0^i is the height of the barrier (or depth of the well), F_0^i is the dc bias field, V_1^i is a homogeneous potential modulation, and F_1^i is a uniform oscillating electric field. Equation (4) includes both the homogeneous and dipole-type oscillations for convenience. For a given region, either V_1 or F_1 will be zero. We use a *single-electron* model and therefore neglect the charging effect as well as imperfections. We shall see that even with this approximation we can obtain qualitative agreement with experiments.

The Floquet theorem asserts that the Schrödinger equation (3) with a time-periodic potential $V(x,t)=V(x,t+T)$ ($T=2\pi/\omega$ is the oscillating period) has solutions of the form:[17]

$$\psi_F(x,t)=e^{-iE_Ft/\hbar}\phi(x,t), \tag{5}$$

where E_F is the Floquet eigenenergy and $\phi(x,t)$ is a periodic function: $\phi(x,t)=\phi(x,t+T)$. Taking the Fourier expansion of $\phi(x,t)$, Eq. (5) becomes:

$$\psi_F(x,t)=e^{-iE_Ft/\hbar}\sum_{n=-\infty}^{\infty}\phi_n(x)e^{-in\omega t}, \tag{6}$$

with the Fourier component

$$\phi_n(x)=\frac{1}{2\pi}\int_0^{2\pi}\phi(x,t)e^{in\omega t}d(\omega t). \tag{7}$$

Equation (6) can also be written as

$$\psi_F(x,t)=\sum_{n=-\infty}^{\infty}\phi_n(x)e^{-iE_nt/\hbar}, \tag{8}$$

where $E_n=E_F+n\hbar\omega$ is the nth Floquet sideband energy. These general statements can be used for our model.

Let us consider a specific region with the potential as in Eq. (4). It is known that the solution of the Schrödinger equation with an oscillating dipole term is the so-called Volkov state[19] used in laser physics. Based on the methods in Ref. 19, an analytic solution for the potential in Eq. (4) can be derived (see the Appendix). For simplicity, in the following equation the index i has been dropped:

$$\begin{aligned}\psi(x,t)=e^{-i(E^0+e^2F_1^2/4\mu\omega^2)t/\hbar}\sum_{l=-\infty}^{\infty}&[a_l\,\mathrm{Gi}^{(+)}(x,t)\\&+b_l\,\mathrm{Gi}^{(-)}(x,t)]\\&\times\exp\left(-il\omega t-\frac{ieF_1x\,\sin(\omega t)}{\hbar\omega}+\frac{ie^2F_1^2\,\sin(2\omega t)}{8\hbar\mu\omega^3}\right.\\&\left.-\frac{ie^2F_0F_1\,\sin(\omega t)}{\hbar\mu\omega^3}-\frac{iV_1\,\sin(\omega t)}{\hbar\omega}\right),\end{aligned} \tag{9}$$

where E^0 is an energy constant, $\mathrm{Gi}^{(\pm)}(x,t)$ denotes

$$\begin{aligned}\mathrm{Gi}^{\pm}(x,t)=\mathrm{Gi}^{(\pm)}\left[\left(\frac{2\mu eF_0}{\hbar^2}\right)^{1/3}\right.\\\left.\times\left(x-\frac{eF_1\cos(\omega t)}{\mu\omega^2}-\frac{E^0-V_0}{eF_0}\right)\right].\end{aligned} \tag{10}$$

$\mathrm{Gi}^{(\pm)}$ are any two linearly independent combinations of the Airy functions Ai and Bi. We will use $\mathrm{Gi}^{(\pm)}=\sqrt{\pi}(\mathrm{Ai}\pm i\,\mathrm{Bi})$ so that they correspond to right and left propagating modes, respectively.

Equation (9) can be written in Floquet format. The summation in Eq. (9) corresponds to the time-periodic function $\phi(x,t)$ in Eq. (5), and the Floquet energy is given by

$$E_F=E^0+\frac{e^2F_1^2}{4\mu\omega^2}. \tag{11}$$

Equation (11) involves F_1 (the dipole oscillation magnitude) but not V_1 (the homogeneous oscillation magnitude). This feature creates extra problems when solving systems with multiple oscillation types. However, we can use the fact that the Floquet energies must be the same in every region, regardless of the type of oscillation; therefore a single Floquet eigenstate characterizes the whole space. This gives us a means to match the states at the boundaries. For an open system with an incident wave of energy E_{in}, the Floquet energy is determined by this incident energy ($E_F=E_{in}$), as shown in Fig. 1.

Once the Floquet energy is determined, we can match the boundary conditions for each Floquet channel by requiring that each ϕ_n in Eq. (8) and its first derivative be continuous at the interfaces. To show a concrete expression for ϕ_n, let us consider the simple case $F_0=0$. The wave function in Eq. (9) is now simplified to

$$\begin{aligned}\psi(x,t)=e^{(-i/\hbar)E_Ft}\sum_{l=-\infty}^{\infty}&[a_le^{iq_l[x-eF_1\cos(\omega t)/\mu\omega^2]}\\&+b_le^{-iq_l[x-eF_1\cos(\omega t)/\mu\omega^2]}]\\&\times\exp\left(-il\omega t-\frac{ieF_1x\sin(\omega t)}{\hbar\omega}+\frac{ie^2F_1^2\sin(2\omega t)}{8\hbar\mu\omega^3}\right.\\&\left.-\frac{iV_1\sin(\omega t)}{\hbar\omega}\right),\end{aligned} \tag{12}$$

where

$$\frac{\hbar^2 q_l^2}{2\mu}=\left(E_F-\frac{e^2F_1^2}{4\mu\omega^2}\right)+l\hbar\omega-V_0. \tag{13}$$

Using the identities $\exp[-iz\sin(\omega t)]=\Sigma_m J_m(z)\exp(-im\omega t)$ and $\exp[-iz\cos(\omega t)]=\Sigma_m(-i)^m J_m(z)\exp(-im\omega t)$, where $J_m(z)$ is the Bessel function of the first kind, Eq. (12) can be written as

$$\psi(x,t)=\sum_{n=-\infty}^{\infty}\sum_{l=-\infty}^{\infty}\sum_{\alpha=-\infty}^{\infty}\sum_{\beta=-\infty}^{\infty}[a_l A_\alpha^+(x)+b_l A_\alpha^-(x)]\times J_\beta\left(\frac{e^2F_1^2}{8\hbar\mu\omega^3}\right)J_{n-l-\alpha+2\beta}\left(\frac{eF_1x}{\hbar\omega}+\frac{V_1}{\hbar\omega}\right)\times\exp\left[-\frac{i}{\hbar}E_n t\right], \tag{14}$$

with

$$A_\alpha^\pm(x)=\exp(\pm iq_l x)\left[(-i)^\alpha J_\alpha\left(\pm\frac{eF_1}{\mu\omega^2}\right)\right]. \tag{15}$$

Equation (14) is now in the Floquet format, as can be easily seen by comparing it to Eq. (8). If we express $\phi_n(x)$ as

$$\phi_n(x)=\sum_{l=-\infty}^{\infty}\phi_{nl}^+(x)a_l+\phi_{nl}^-(x)b_l, \tag{16}$$

we have

$$\phi_{nl}^\pm(x)=\sum_{\alpha=-\infty}^{\infty}\sum_{\beta=-\infty}^{\infty}A_\alpha^\pm(x)J_\beta\left(\frac{e^2F_1^2}{8\hbar\mu\omega^3}\right)\times J_{n-l-\alpha+2\beta}\left(\frac{eF_1x}{\hbar\omega}+\frac{V_1}{\hbar\omega}\right). \tag{17}$$

Similarly when $F_0\neq 0$ we can derive ϕ_{nl} as well as ϕ_n, with $A_\alpha^\pm(x)$ in Eq. (15) replaced by the αth Fourier coefficient of $\mathrm{Gi}(x,t)$ in Eq. (10). We obtain $A_\alpha^\pm(x)$ numerically for this case.

Now we have the wave function for each region i:

$$\psi^{(i)}(x,t)=\sum_{n=-\infty}^{\infty}\sum_{l=-\infty}^{\infty}[\phi_{nl}^{+(i)}(x)a_l^{(i)}+\phi_{nl}^{-(i)}(x)b_l^{(i)}]e^{(-i/\hbar)E_n t}. \tag{18}$$

The first derivative of this wave function can be obtained by taking the derivative of $\phi_{nl}(x)$ in Eq. (17) with respect to x to get $\phi_{nl}'^{+}(x)$.

To determine the coefficients $a_l^{(i)}$ and $b_l^{(i)}$, we adapt the commonly used transfer matrix technique,[10] and then construct the Floquet S matrix,[13] as will be briefly discussed below. Consider an interface x_i with wave function $\psi^{(i)}(x,t)$ on the left side and $\psi^{(i+1)}(x,t)$ on the right. The transfer matrix $\mathbf{M}(x_i)$ gives the following transformation of wave coefficients:

$$\begin{pmatrix}\mathbf{a}^{(i+1)}\\ \mathbf{b}^{(i+1)}\end{pmatrix}=\mathbf{M}(x_i)\begin{pmatrix}\mathbf{a}^{(i)}\\ \mathbf{b}^{(i)}\end{pmatrix}. \tag{19}$$

The matrix $\mathbf{M}(x_i)$ in Eq. (19) is obtained from the condition that the wave function and its first derivative be continuous at the interface x_i. This gives

$$\mathbf{M}(x_i)=[\mathbf{m}(x_i)]_{(i+1)}^{-1}[\mathbf{m}(x_i)]_{(i)}, \tag{20}$$

with

$$[(\mathbf{m}(x_i)]_{(\text{region } i)}=\begin{pmatrix}\boldsymbol{\phi}_{nl}^+(x_i) & \boldsymbol{\phi}_{nl}^-(x_i)\\ \boldsymbol{\phi}_{nl}'^+(x_i) & \boldsymbol{\phi}_{nl}'^-(x_i)\end{pmatrix}_{(\text{region } i)}. \tag{21}$$

In Eq. (20) the subscripts (i) and $(i+1)$ denote the side of the interface x_i where the evaluation is performed.

The total transfer matrix is the product of $\mathbf{M}(x_i)$ from each interface:

$$\mathbf{M}_{transfer}=\prod_i \mathbf{M}(x_i). \tag{22}$$

The matrix $\mathbf{M}_{transfer}$ connects the Floquet coefficients between the leftmost region and the rightmost region. Furthermore, $\mathbf{M}_{transfer}$ can be used to construct the matrix $\mathcal{S}$, which connects the incoming and outgoing waves directly:[13]

$$\begin{pmatrix}\mathbf{a}^{(out)}\\ \mathbf{b}^{(out)}\end{pmatrix}=\mathcal{F}\begin{pmatrix}\mathbf{a}^{(in)}\\ \mathbf{b}^{(in)}\end{pmatrix}, \tag{23}$$

where $\mathbf{a}^{(in)},\mathbf{b}^{(in)}$ and $\mathbf{a}^{(out)},\mathbf{b}^{(out)}$ are the incoming and outgoing amplitude vectors (including the associated evanescent Floquet sidebands[13]), respectively. If we keep only the part of matrix $\mathcal{F}$ that connects incoming *propagating* modes and outgoing *propagating* modes, we can obtain the scattering S matrix, as discussed in detail in Ref. 13:

$$\overline{S}=\begin{pmatrix}\overline{r} & \overline{t'}\\ \overline{t} & \overline{r'}\end{pmatrix}, \tag{24}$$

where $\overline{r}$, $\overline{t}$, $\overline{t'}$, and $\overline{r'}$ are the matrixes whose elements r_{nm} and t_{nm} are the reflection and transmission amplitudes, respectively, for *propagating* modes incident from the left; r'_{nm} and t'_{nm} are similar quantities for *propagating* modes incident from the right. [Note the **S** in Eq. (2) connects amplitudes of incoming to outgoing. The usual S matrix, **S**, which connects incoming current to outgoing current is given by $\mathbf{S}=N^{-1}\mathbf{S}N$, where N is a diagonal normalization matrix. For the case of Fig. 1, it has a matrix element $N_{nn}=1/\sqrt{k_n}$, where k_n is the wave vector of the nth Floquet channel.]

From the transmission amplitudes we can calculate the transmission coefficient T. For example, considering a single electron beam with a fixed energy E_I incident from one side, say the left, we have

$$T=\sum_l \frac{\gamma_l^{(out)}}{\gamma_I^{(in)}}|t_{lI}|^2, \tag{25}$$

where t_{lI} is the transmission amplitude and $\gamma_l^{(out)}/\gamma_I^{(in)}$ is a ratio between the incident and the l th transmitted modes. For the simple static scattering case with plane waves in both the incoming and outgoing regions, $\gamma_l^{(out)}/\gamma_I^{(in)}$ is the familiar $k^{(out)}/k^{(in)}$, the ratio between the incoming and outgoing

wave vectors. When the outgoing region undergoes homogeneous oscillation as in Fig. 1, as will be derived later in Eq. (30),

$$\frac{\gamma_l^{(out)}}{\gamma_I^{(in)}} = \sum_{n=-\infty}^{\infty} \frac{k_l^{(out)}}{k_I^{(in)}} J_{n-l}^2\left(\frac{V_1}{\hbar\omega}\right). \tag{26}$$

From T we can calculate the transmission current. Consider first the contribution to the current due to the incident electrons with wave vector $\mathbf{k}^{(in)}$ (denoting the x component by $k_I^{(in)}$), with a corresponding electron density n. The current density can be written

$$\mathbf{j}(\mathbf{r},t) = ne\left[\frac{i\hbar}{2\mu}[\Psi(\mathbf{r},t)\nabla\Psi^*(\mathbf{r},t) - \Psi^*(\mathbf{r},t)\nabla\Psi(\mathbf{r},t)]\right], \tag{27}$$

and we neglect the reverse current, namely the current from the collector to the emitter, since it is normally much smaller.

What we measure in the experiment is the x component of the current. From Eqs. (2) and (27), this can be deduced from the 1D wave function [with the transverse part $\phi(y,z,t)$ in Eq. (2) normalized]:

$$j_x(x,t) = ne\frac{i\hbar}{2\mu}\left(\psi(x,t)\frac{\partial}{\partial x}\psi^*(x,t) - \psi^*(x,t)\frac{\partial}{\partial x}\psi(x,t)\right). \tag{28}$$

In the collector region, under the homogeneous oscillation with a modulation strength V_1 (see Fig. 1), the wave function is simply[13]

$$\psi(x,t) = \sum_{l=-\infty}^{\infty}\sum_{n=-\infty}^{\infty} t_{lI} e^{ik_l^{(out)}x} J_{n-l}\left(\frac{V_1}{\hbar\omega}\right) e^{(-i/\hbar)E_n t}. \tag{29}$$

Substituting this wave function into Eq. (28), the average current over one oscillation period is

$$\begin{aligned} j_x &= ne\frac{\hbar}{\mu}\sum_{l=-\infty}^{\infty}\sum_{n=-\infty}^{\infty} k_l^{(out)} J_{n-l}^2\left(\frac{V_1}{\hbar\omega}\right)|t_{lI}|^2 \\ &= ne\frac{\hbar k_I^{(in)}}{\mu}\sum_{l=-\infty}^{\infty}\left[\sum_{n=-\infty}^{\infty}\frac{k_l^{(out)}}{k_I^{(in)}} J_{n-l}^2\left(\frac{V_1}{\hbar\omega}\right)\right]|t_{lI}|^2 \\ &= ne\frac{\hbar k_I^{(in)}}{\mu}\sum_l\left[\frac{\gamma_l^{(out)}}{\gamma_I^{(in)}}\right]|t_{lI}|^2 = ne\frac{\hbar k_I^{(in)}}{\mu}T, \end{aligned} \tag{30}$$

where we use the definitions of T and $\gamma_l^{(out)}/\gamma_I^{(in)}$ as in Eqs. (25) and (26).

Equation (30) gives the transmission current due to the incident electrons with a single wave vector. The total current involves the contribution from all the incident electrons:

$$J_x = e\int\int\int_0^{\infty} d\mathbf{k} D(\mathbf{k})\frac{\hbar k_x}{\mu}T(k_x). \tag{31}$$

$D(\mathbf{k}) = D(k_x,k_y,k_z)$ is the incident electron density of state, which is a function of k_x, k_y, and k_z, so in general in the integration above the transversal motion should be taken into account.

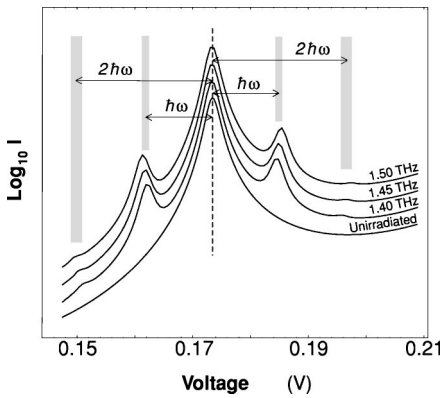

FIG. 2. I-V traces (with vertical offsets) of a triple-barrier–double-well structure with terahertz radiations (using 0.2 eV as the barrier height and 0.02 mV/Å as the oscillating field strength). Satellite peaks show the photon-assisted tunnelings. Both single- and double-photon processes (as indicated by arrows) are visible.

In this paper, we will calculate the I-V curve for two special cases, namely a double barrier resonant tunneling structure (DBRTS) as well as a triple-barrier case, where we follow a very simple yet qualitatively effective technique discussed in Ref. 20. (Some general treatments for evaluating the current have been discussed in the literature, see, for example Refs. 2, 6, and 7.) For this type of configuration, by applying the dc bias, electrons accumulate at the emitter-barrier interface and form a two-dimensional electron gas (2DEG). They are free to move in the transverse plane but the spatial confinement quantizes the energy associated with the motion in the x direction. The lowest energy level is mostly populated[20] and we denote it as E_B. The corresponding x component of the wave vector is $k_B = \sqrt{2\mu E_B}/\hbar$. So without doing the integration in Eq. (31), the current is simply

$$\begin{aligned} J &= e\frac{\hbar k_B}{\mu}T(E_B)\left[\int_0^{\infty}\int_0^{\infty} dk_y dk_z D(k_B,k_y,k_z)\right] \\ &= Ne\frac{\hbar k_B}{\mu}T(E_B) = Ne\sqrt{\frac{2E_B}{\mu}}T(E_B), \end{aligned} \tag{32}$$

where N is the density of electrons in the 2DEG, and T is the transmission coefficient corresponding to energy E_B, which is obtained using the *Fang-Howard* model[21] for the potential variation through the device.[20] We'll give a comparison of our numerical results with the experiments in the following section.

III. COMPARISON WITH PHOTON-ASSISTED-TUNNELING EXPERIMENTS

In Fig. 2, the I-V curve [current I is given by the current density J in Eq. (32) and V is the potential drop between the emitter and collector regions] shows clearly the photon-assisted-tunneling in a driven resonant tunneling diode (RTD), as observed in the experiment.[3] The semiconductor structure considered here, as reported in Ref. 3, consists of a $Al_{0.3}Ga_{0.7}As$ triple barrier (with widths 35 Å, 60 Å, and 35 Å) separated by a GaAs double well (180 Å and 100 Å). When coupled to a terahertz radiation through a bowtie an-

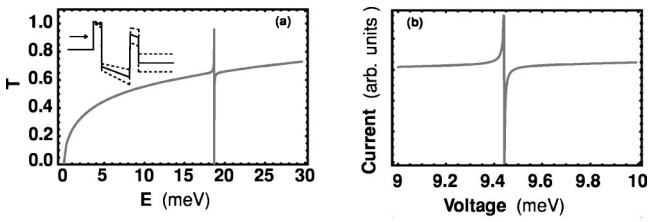

FIG. 3. (a) Bound-state-induced transmission resonance of a DBRTS. The parameters are boundaries $x_i=\{0,15,85,100\}$ Å, $F_0=\{0,-0.1,-0.1,-0.1,0\}$ mV/Å, $V_0=\{0,40,-30,40,-10\}$ meV, $\hbar\omega=30$ meV, $F_1=\{0,0.02,0.02,0.02,0\}$ mV/Å, and $V_1=\{0,0,0,0,2\}$ meV. (b) The dynamic resonance appears in the current-voltage characteristic.

tenna, the frequency-dependent satellite current peaks appear, surrounding the original resonant tunneling peak. Our results agree well with the experiments. The *I-V* analysis for the same experiment was also obtained in Ref. 7 using a sequential current model including the charging effect, where the oscillation type is considered to be homogeneous in each region, with the oscillation strength taken to be the average strength in that region.

In the remainder of this paper, we will focus on a different resonant transport mechanism, where in general we need a heterostructure, which in the absence of an oscillating field has true bound states.

IV. BOUND-STATE-INDUCED DYNAMIC TRANSMISSION RESONANCE

Figure 3(a) shows the transmission probability for a driven DBRTS, with a quantum well involved (made of semiconductor material like $In_xGa_{1-x}As$). We notice that an asymmetric ''Fano'' type transmission resonance (involving a transmission peak as well as a dip) appears approximately at $E=18.7$ meV. This resonance results from the transition and interference of electrons among Floquet channels due to the interaction of the electrons with the oscillating field. In the absence of the field, this DBRTS has a bound state at $E_b=-11.3$ meV. When the incident energy is one photon energy higher than the bound-state energy,

$$E-E_b=\hbar\omega, \tag{33}$$

the electrons are able to transit to and accumulate in the relatively long-lived bound state by means of photon emission, and also to transfer back from the bound state to the propagating channels by photon absorption, forming the Floquet asymmetric transmission resonance. From this example, we see that according to Eq. (33), the bound-state energy can be detected by locating the Floquet transmission resonance. Thus, Floquet resonances can be used to ''probe'' the semiconductor energy spectrum, and measure material structure parameters such as thickness and band gaps. In addition, this sharp peak-dip resonance pattern (sometimes only a dip appears, and generally much narrower than the static transmission resonance peak and PAT resonance peak) also allows sensitive control of the current and may be useful for designing fast response switching devices in quantum computation. Figure 3(b) shows how this dynamic resonance can be detected from the *I-V* measurement.

Equation (33) also holds when there is more than one bound state, as shown in Fig. 4(a). The three Floquet resonances at $E=2.074$, 3.747, 6.307 meV correspond to the three bound states at $E_b=-5.927$, -4.255, -1.694 meV, respectively. Figure 4(b) also shows that at each resonance, the scattering electrons undergo delays as measured by the Wigner delay time,[13] implying the trapping of electrons by the driven quantum well. Another quantity, of the same order of magnitude as the Wigner delay time, is the lifetime calculated from the Floquet quasibound states. Quasibound states appear as *S*-matrix poles in the complex energy plane, as shown in Fig. 4(d). The lifetime is determined by the imaginary part of the quasienergy. The three transmission resonances in Fig. 4(a) have three corresponding transmission poles (with a transmission amplitude zero associated with each of them). Figure 4(d) also shows one static pole, which is the farthest one from the real energy axis, corresponding to the broad static transmission resonance centered around 1.3 meV in Fig. 4(a).

Figure 5 compares the transmission patterns of two types of oscillations. The parameters are chosen in such a way that inside the well, the homogeneous oscillation strength in Fig. 5(b) is equal to the average dipole oscillation strength of Fig. 5(a): $V_1^b=V_{av}^a=eF_1L/2$, where L is the width of the quantum well. The resonance widths for the dipole oscillations in Fig. 5(a) are generally broader than those for the homogeneous

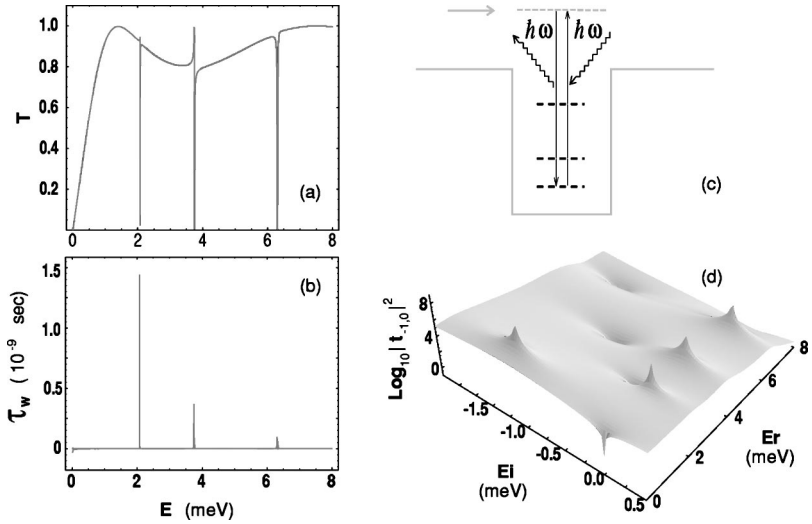

FIG. 4. Transmission resonances (a) due to three bound states and (b) the Wigner delay time. (c) sketches the bound states and electron transition processes. The parameters are $\hbar\omega=8$ meV, $x_i=\{0,800\}$ Å, $V_0=\{0,-6.5,0\}$ meV, $F_1=\{0,0.002,0\}$ mV/Å. (d) shows the transmission poles in the complex energy plane ($t_{-1,0}$ is the transmission amplitude from the incident channel to the nearest lower Floquet channel).

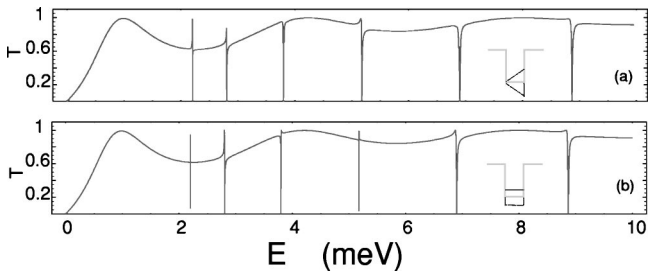

FIG. 5. Comparison of the transmission resonances due to two types of oscillations. The dipole oscillation in (a) has the average strength as the homogeneous oscillation in (b) but gives broader resonances. Parameters of the quantum well are $x_i=\{0,1500\}$ Å and $V_0=\{0,-8,0\}$ meV. $\hbar\omega=10$ meV; the oscillation strengths are (a) $F_1=\{0,0.002,0\}$ mV/Å; (b) $V_1=\{0,1.5,0\}$ meV.

oscillation in Fig. 5(b). This is most obvious for the resonances at $E=2.2$ meV and $E=5.2$ meV, which shows that the dipole oscillation enhances the interband transition and makes the system more unstable. A more accurate quantitative comparison (not shown) can be obtained from the Wigner delay times as well as the lifetimes of the quasibound states.

A small yet finite change of the quasibound state energy when varying the oscillating field strength is also observed. Figure 6 shows this ac Stark quasibound energy shift, $\Delta E_{quasibound}$ [the quasibound state considered here corresponds to the fourth Floquet resonance in Fig. 5(a)]. Both the real and imaginary parts of its energy vary quadratically with F_1,

$$\Delta E_{quasibound} \propto F_1^2. \tag{34}$$

This shift will consequently change the dynamic resonance location, as governed by Eq. (33). In the meantime, the regular resonant tunneling, such as the central resonance in Fig. 2, is determined by the quasibound energy inside the quantum well,[20] so should also follow this change. An oscillation-strength-dependent resonance shift is clearly seen in the experimental *I-V* curves of Ref. 3. However, other factors, like heating and charging effects, contribute also to the resonance shift, as been discussed in Refs. 3 and 7.

V. CONCLUSION

In conclusion, we presented above a generic Floquet scattering approach that allows us to obtain the Floquet eigenstates and the *S* matrix for systems with many scattering regions and with multiple oscillation types involved. Our results agree with the photon-assisted-tunneling experiments. We have discussed the behaviors of several different driven heterostructures, and we propose experiments that can be done to observe bound-state-induced dynamic transmission resonances.

ACKNOWLEDGMENTS

The authors wish to thank the Welch Foundation, Grant No. F-1051, NSF Grant No. INT-9602971, and DOE Contract No. DE-FG03-94ER14405 for partial support of this work. We also thank NPACI and the University of Texas at Austin High Performance Computing Center for use of their computer facilities and Professor R. van de Geijn for programming assistance in parallel computing. We thank Agapi Emmanouilidou, Biao Wu and Han Htoon for helpful discussions.

APPENDIX: SOLUTION OF THE SCHRÖDINGER EQUATION

Although the solution of the Schrödinger equation with a dipole oscillation term is discussed in Ref. 19, to make this paper self-contained, in this Appendix we give a brief derivation of the wave function, Eq. (9).

Let us write the potential [see Eq. (4), we drop the *i* in this Appendix] $V(x,t)=g(x,t)+xf(t)$, with $g(x,t)=V_0+eF_0x+V_1\cos(\omega t)$ and $f(t)=eF_1\cos(\omega t)$; we also define $p(t)=\int^t dt' f(t')$. From Ref. 19, the wave function can be decomposed into $\psi(x,t)=\Phi(\xi,t)\chi(x,t)$, where

$$\xi = x+\frac{1}{\mu}\int^t dt' p(t') = x-\frac{eF_1}{\mu\omega^2}\cos(\omega t), \tag{A1}$$

$$\chi(x,t)=\exp\left(-\frac{i}{\hbar}\left[Et+xp(t)+\int^t dt'\frac{p^2(t')}{2\mu}\right]\right)$$
$$=\exp\left(-\frac{i}{\hbar}Et-\frac{ieF_1x\sin(\omega t)}{\hbar\omega}+\frac{ie^2F_1^2\sin(2\omega t)}{8\hbar\mu\omega^3}\right). \tag{A2}$$

After substituting $\psi(x,t)$ into the Schrödinger equation (3), we obtain the following equation for $\Phi(\xi,t)$:

$$i\hbar\frac{\partial}{\partial t}\Phi(\xi,t)=-\frac{\hbar^2}{2\mu}\frac{\partial^2}{\partial\xi^2}\Phi(\xi,t)$$
$$+\left[V_0-E+eF_0\xi\right.$$
$$\left.+\left(V_1+\frac{e^2F_0F_1}{\mu\omega^2}\right)\cos(\omega t)\right]\Phi(\xi,t). \tag{A3}$$

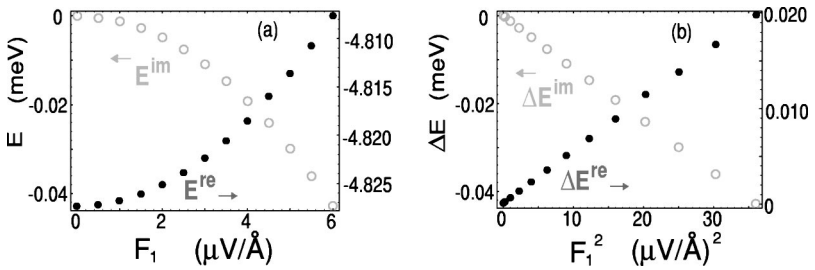

FIG. 6. ac Stark energy shifts. (a) shows that the energy changes slightly when a static bound state (when $F_1=0$) is driven into quasibound state by the oscillating field. (b) shows that the changing amount is proportional to the square of F_1. This relation holds for both the real (●) and imaginary (○) parts.

Equation (A3) involves only a homogeneous modulation term so it can be easily solved. Let

$$\Phi(\xi,t)=\varphi(\xi)\exp\left[-\frac{i}{\hbar\omega}\left(V_1+\frac{e^2F_0F_1}{\mu\omega^2}\right)\sin(\omega t)\right]. \tag{A4}$$

$\varphi(\xi)$ is the solution of the time-independent Schrödinger equation:

$$E\varphi(\xi)=-\frac{\hbar^2}{2\mu}\frac{\partial^2}{\partial\xi^2}\varphi(\xi)+(V_0+eF_0\xi)\varphi(\xi). \tag{A5}$$

We know when $F_0=0,\varphi(\xi)$ corresponds to the spatial part of a plane wave, while in general when $F_0\neq 0$ the solution consists of Airy functions.

[1] P. Guimarães *et al.*, Phys. Rev. Lett. **70**, 3792 (1993).
[2] V.A. Chitta *et al.*, J. Phys.: Condens. Matter **6**, 3945 (1994).
[3] H. Drexler *et al.*, Appl. Phys. Lett. **67**, 2816 (1995).
[4] T.H. Oosterkamp *et al.*, Phys. Rev. Lett. **78**, 1536 (1997), and references therein.
[5] H.C. Liu, Phys. Rev. B, **43**, 12 538 (1991).
[6] J. Iñarrea *et al.*, Phys. Rev. B, **50**, 4581 (1994); **51**, 5244 (1995); R. Aguado *et al.*, *ibid.*, **53**, 10 030 (1996); J. Iñarrea *et al.*, Europhys. Lett. **40**, 417 (1997); R. Aguado *et al.*, Phys. Rev. Lett. **81**, 4971 (1998).
[7] R. Aguado *et al.*, Phys. Rev. B, **55**, 12 860 (1997).
[8] C. Perez del Valle *et al.*, Phys. Rev. A **59**, 3701 (1999).
[9] I. Vorobeichik *et al.*, Europhys. Lett. **41**, 111 (1998); Phys. Rev. A **59**, 1699 (1999); **59**, 2511 (1999).
[10] M. Wagner, Phys. Rev. Lett. **76**, 4010 (1996); Phys. Rev. B **55**, R10 217 (1997); **57**, 11 899 (1998).
[11] M. Henseler, T. Dittrich, and K. Richter, (unpublished).
[12] C.S. Tang and C.S. Chu, Phys. Rev. B **60**, 1830 (1999).
[13] Wenjun Li and L.E. Reichl, Phys. Rev. B **60**, 15 732 (1999), and references therein.
[14] A. Ignatov *et al.*, J. Appl. Phys. **85**, 3643 (1999).
[15] M. Switkes, C.M. Marcus, K. Campman, and A.C. Gossard, Science **283**, 1905 (1999).
[16] M. Büttiker, (unpublished).
[17] J.H. Shirley, Phys. Rev. **138**, B979 (1965).
[18] We will concentrate mainly on the undopped scattering regions.
[19] K. Husimi, Prog. Theor. Phys. **9**, 381 (1953); F.H. Kerner, Can. J. Phys. **36**, 371 (1958); D. ter Haar, *Problems in Quantum Mechanics*, 3rd ed., (Pion, London, 1975), p. 17; W.S. Truscott, Phys. Rev. Lett. **70**, 1900 (1993).
[20] P.B. Wilkinson *et al.*, Nature (London) **380**, 608 (1996); T.M. Fromhold *et al.*, Phys. Rev. Lett. **75**, 1142 (1995).
[21] F.F. Fang and W.E. Howard, Phys. Rev. Lett., **16**, 797 (1966).